Tunable Polymer Nanoreactors from RAFT Polymerization-Induced Self-Assembly: Fabrication of Nanostructured Carbon-Coated Anatase as Battery Anode Materials with Variable Morphology and Porosity

*Yen Theng Cheng,[1,3] Qingbo Xia,[2,3] Hongwei Liu,[4] Marcello B. Solomon,[2] Emma R. L. Brisson,[1] Lewis D. Blackman,[5] Chris D. Ling,[2,3] Markus Müllner[1,3,]**

[1]Key Centre for Polymers and Colloids, School of Chemistry, The University of Sydney, Sydney, NSW 2006, Australia; [2]School of Chemistry, The University of Sydney, Sydney, NSW 2006, Australia; [3]The University of Sydney Nano Institute (Sydney Nano), Sydney, NSW 2006, Australia; [4]Sydney Microscopy & Microanalysis, the University of Sydney node of Microscopy Australia, Sydney, NSW 2006, Australia; [5]CSIRO Manufacturing Business Unit, Research Way, Clayton, VIC 3168, Australia.

Keywords. RAFT polymerization, block copolymers, polymer templating, nanocrystalline TiO_2, nanocomposites

Abstract

We demonstrate a modular synthesis approach to yield mesoporous carbon-coated anatase (denoted as TiO_2/C) nanostructures. Combining polymerization-induced self-assembly (PISA) and reversible addition-fragmentation chain transfer (RAFT) dispersion polymerization enabled the fabrication of uniform core-shell polymeric nanoreactors with tunable morphology. The nanoreactors comprised of a poly(2-(dimethylamino)ethyl methacrylate) (PDMAEMA) shell and a poly(benzyl methacrylate) (PBzMA) core. We selected worm-like and vesicular morphologies to guide the nanostructuring of a TiO_2 precursor, namely titanium(IV) *bis*(ammonium lactato)dihydroxide) (TALH). Subsequent carbonization yielded nanocrystalline anatase and simultaneously introduced a porous carbon framework, which also suppressed the crystal growth (~5 nm crystallites). The as-prepared TiO_2/C materials comprised of a porous structure, with large specific surface areas (>85 m^2/g) and various carbon contents (20–30 wt%). As anode components in lithium-ion batteries, our TiO_2/C nanomaterials improved the cycling stability, facilitated high overall capacities, and minimised the capacity loss compared to both their *sans*-carbon and commercial anatase analogues.

Introduction

Metal oxides are an important class of materials with their extensive use across a range of energy-storing,[1] photocatalytic,[2] gas sensing,[3] and biomedical[4] applications. Tin oxides (SnO and SnO_2),[5] niobium oxides (NbO, Nb_2O_5),[6] and titanium dioxide (TiO_2),[7–9] especially have been studied extensively as their band gaps, high dielectric constants, thermal and chemical stabilities attest them desirable properties in these applications. In this context, nanostructured metal oxides display superiority over their bulk counterparts in terms of enhanced electron or ion diffusivity, storage and cycling stability, which stems largely from their high surface-to-volume ratios and tuneable confined dimensions within the materials. Several synthesis routes to nanostructured inorganics have been developed, including electrospinning,[10] solvo/hydrothermal processes[11] and soft/hard templating.[7–9,12] In addition, soft-templating routes employ predominately organic templates (such as surfactants[13] and block copolymers[12,14]) as structure-directing agents to direct precursors of inorganic materials into predictable morphologies, compositions and porosities. Diverse morphologies, such as nanofibres/nanotubes,[15,16] porous microparticles[17,18] hierarchically porous microspheres,[19] ordered mesostructured films,[20–22] and carbon-coated mesoporous nanospheres can thereby be achieved.[23] Most syntheses of these structure-directing soft templates are based on traditional self-assembly (such as solvent switch methods) typically conducted in extremely dilute solutions (~1 wt % solid content), making large scale production challenging.[24]

Polymerization-induced self-assembly (PISA) has emerged as a facile one pot method to produce high-fidelity polymer nanoparticles at high solid content (20–50 wt.%) without the need for extensive purification.[25–28] PISA allows for accessing the full phase diagram, which grants formidable morphology control in polymer nanoparticle (*i.e.* template) fabrication.[29–32] Several

studies highlighted the usefulness of PISA to various applications, including spherical PISA nanoparticles as catalyst supports,[33,34] or PISA vesicles for cargo loading in biomedical applications.[28,35,36] Thermoresponsive PISA nanoparticles also provided an avenue to high-temperature oil thickening.[37] While the value of PISA, especially to biomedical research, has been demonstrated to date, the exploitation of key advantages of the PISA process to produce hybrid and inorganic nanostructures has been scarcely reported. Chang *et al.* used nanoscale PISA spheres to produce hollow titania nanoparticles for photocatalytic degradation studies of methyl orange.[38] Bennett *et al.* used PISA under supercritical CO_2 conditions to produce phase-separated microparticles to yield mesoporous TiO_2 and $LiFePO_4$ microparticles by sol-gel templating.[39] Teo *et al.* used PISA to form silsesquioxane hybrids of different morphologies *in situ* by copolymerizing an alkoxysilane-bearing monomer.[40] Zhang *et al.* used spherical PISA particles to immobilize gold, or silica and titania nanoparticles.[41] While these studies employ PISA to generate polymer templates, the majority of the achieved morphologies are limited to spherical micelles or vesicles. This may be attributed to the narrow region on the PISA phase diagram where worm-like assemblies remain stable, especially in the context of further processing for templating.[42,43] However, Zhang *et al.* has shown that worm-like PISA nanostructures can be transferred to silica nanotubes when using templating based on sol-gel chemistry.[44] Although, the above studies have made early steps in using PISA in soft-templating, they were predominately focussed on sol-gel chemistry, mainly used PISA for already easy-to-access spherical templates, or were motivated by applications in catalysis and biomedicine.

We propose the use of PISA to generate difficult-to-access nanoparticles, and to employ them as versatile and scalable nanoreactor templates to synthesize mesoporous carbon-coated anatase TiO_2 (TiO_2/C) nanostructures (Figure 1). As TiO_2 remains a desirable component for battery

research,[45,46] with carbon-coated TiO_2 as a promising anode material in lithium-ion batteries (LIBs),[19,47,48] we seek to highlight the potential of nanostructuring and morphology control in anatase hybrids to enhance their performance. Our PISA nanoparticles were prepared *via* reversible addition-fragmentation chain transfer (RAFT) dispersion polymerization and consisted of poly(2-(dimethylamino)ethyl methacrylate)-*block*-poly(benzyl methacrylate) (PDMAEMA-*b*-PBzMA) diblock copolymers. PISA allowed for a straightforward, high solid content production of worm-like and vesicular templates with identical polycationic shell dimensions. Nanostructuring was subsequently achieved by selectively loading a negatively charged and water-soluble anatase precursor, namely titanium(IV) *bis*(ammonium lactate) dihydroxide (TALH), into the PDMAEMA shell. No crosslinking of the polymer templates was required during TALH loading, even for the charged worm-like templates. Upon pyrolysis of the as-synthesised hybrids (at 650 ºC), two simultaneous processes occurred: TALH converted to anatase TiO_2 nano-crystallites, while the polymer template containing sp^2-hybridized PBzMA carbonized and encased the nanocrystallites in a carbon framework that suppressed their growth and sintering. The ability to produce carbon-coated TiO_2 hybrids from worm-like and vesicular templates further enabled a controllable adjustment of the overall morphology and mesoporosity of the nanomaterials. Accessing different morphologies of the hybrid material has proved beneficial in elucidating the effect of template and hybrid morphology on their use as an anode material in LIBs, whereby the small crystallite size and carbon framework improved the overall electrochemical performance, while a worm-like morphology guaranteed an increased lithium storage capacity.

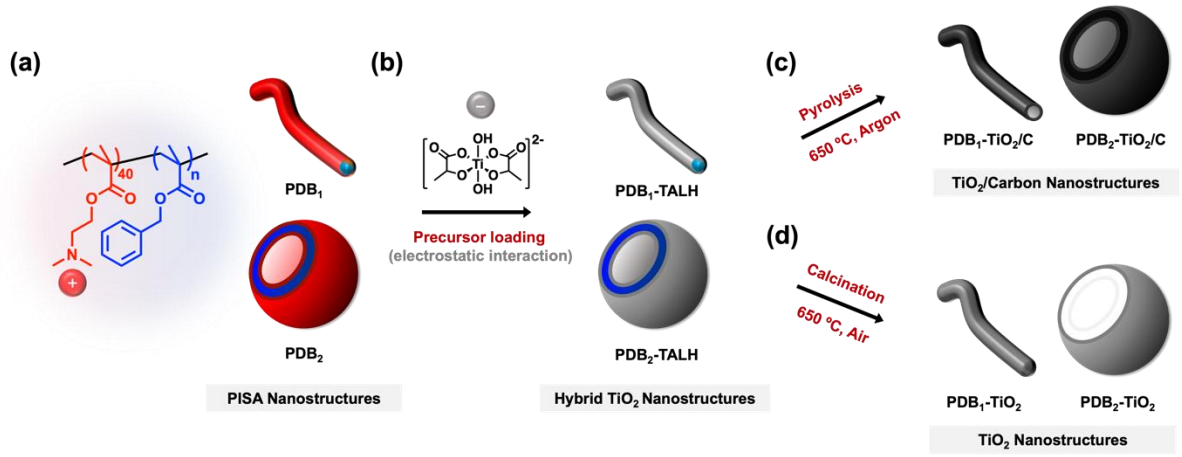

Figure 1. Template-directed synthesis of hollow, worm-like and vesicular anatase TiO_2/C using PISA nanostructures. (a) PISA templates for the worm-like and vesicular morphologies, with the composition of $PDMAEMA_{40}$-*b*-$PBzMA_n$ diblock copolymer (where n = 100 and 200, respectively). (b) Loading of TALH (TiO_2 precursor) to the PDMAEMA domain of the PISA template. (c) Pyrolysis or (d) calcination at 650 ºC to convert TALH to anatase TiO_2 and either simultaneously carbonize the PISA template to create a carbon framework or burn it off to yield a purely inorganic nanomaterial.

Experimental Section

Synthesis of $PDMAEMA_{40}$ macroCTA. A Schlenk flask containing 4-cyano-4-[(dodecylsulfanylthiocarbonyl)sulfanyl]pentanoic acid (CDTPA, 100 mg, 0.248 mmol, DMAEMA (1947.3 mg, 12.4 mmol) and azobisisobutyronitrile (AIBN, 8.1 mg, 0.05 mmol) in isopropanol (12.4 mL) was degassed through three cycles of freeze-pump-thaw, then immersed into an oil bath heated to 70 ºC for 5 h. The polymerization was terminated by exposure to atmospheric air, followed by immersion into liquid nitrogen to completely cool the reaction. The monomer conversion was 79% as determined by ^{1}H NMR spectroscopy in $CDCl_3$. $PDMAEMA_{40}$ was purified by dialysis (MWCO = 2 kDa) in ethanol. The solvent was removed under reduced pressure, followed by drying under high vacuum at room temperature overnight, yielding a yellow product. The product was characterized using ^{1}H NMR spectroscopy and size exclusion chromatography.

Synthesis of $PDMAEMA_{40}$-b-$PBzMA_n$ (PDB) diblock copolymers. In a typical RAFT PISA procedure, $PDMAEMA_{40}$ macroCTA (350 mg, 0.06 mmol), BzMA (835.4 mg, 4.7 mmol) and AIBN (1.95 mg, 0.12 mmol) were dissolved in anhydrous ethanol (6 mL) at 20 wt% solid content in a glass vial. The reaction was degassed under nitrogen flow for 15 min before it was immersed into an oil bath heated to 70 ºC for 24 h. The polymerization was terminated by exposure to atmospheric air, followed by immersion into liquid nitrogen to completely cool the reaction. The monomer conversion was determined by ^{1}H NMR spectroscopy in $CDCl_3$. The purified product was characterized using ^{1}H NMR spectroscopy and DMAc SEC.

Preparation of hybrid PDB_1-TALH and PDB_2-TALH. For the preparation of PDB_1-TALH, PDB_1 (3500 mg, 20 wt% solid content) was immersed in an ethanol/water solution (80% v/v) containing TALH (1933 mg, 6.57 mmol). For the preparation of PDB_2-TALH, PDB_2 (5000 mL,

20 wt% solid content) was added to an ethanol/water solution (50 % v/v) in water containing TALH (1491 mg, 5.07 mmol). The PDB/TALH solutions were left at room temperature for 24 h for TALH infiltration. Excess TALH was removed by dialysis (MWCO = 14 kDa) in ethanol. The residual ethanol was removed by centrifugation and the product was freeze-dried from water to yield a white powder.

Preparation of PDB_1-TiO_2/C, PDB_1-TiO_2, PDB_2-TiO_2/C and PDB_2-TiO_2. PDB_1-TiO_2/C and PDB_2-TiO_2/C were prepared by pyrolysing the corresponding hybrid materials at 650 ºC in a tube furnace under flowing stream of argon for 2 h, with a heating rate of 3 ºC min^{-1}. PDB_1-TiO_2 and PDB_2-TiO_2 were fabricated by calcination of the corresponding hybrid materials in a muffle furnace at 650 ºC in air for 2 h, with a heating rate of 3 ºC min^{-1}.

Results and Discussion

Synthesis of polymeric templates *via* polymerization-induced self-assembly

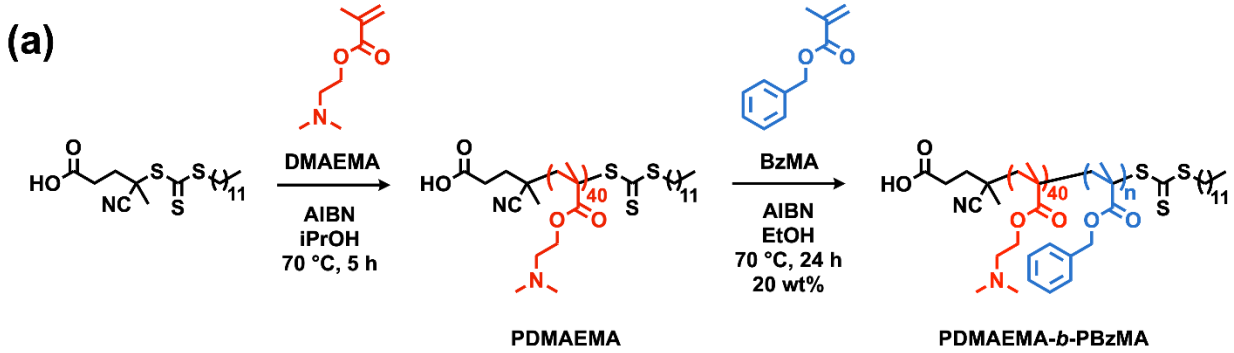

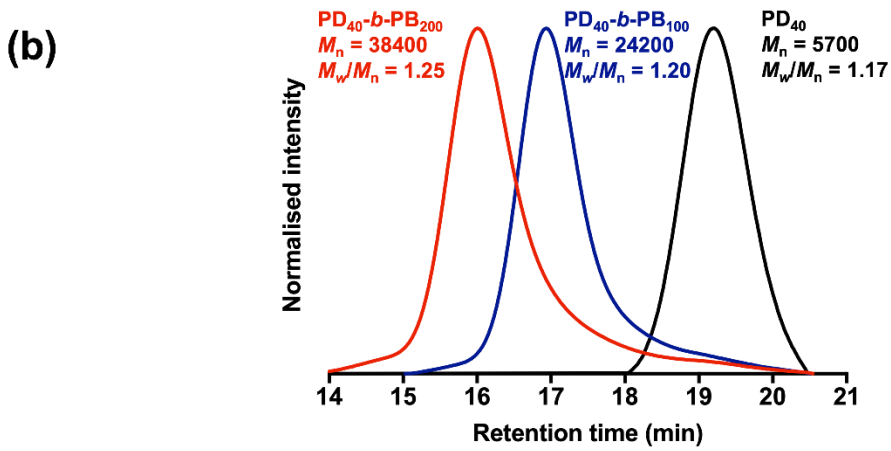

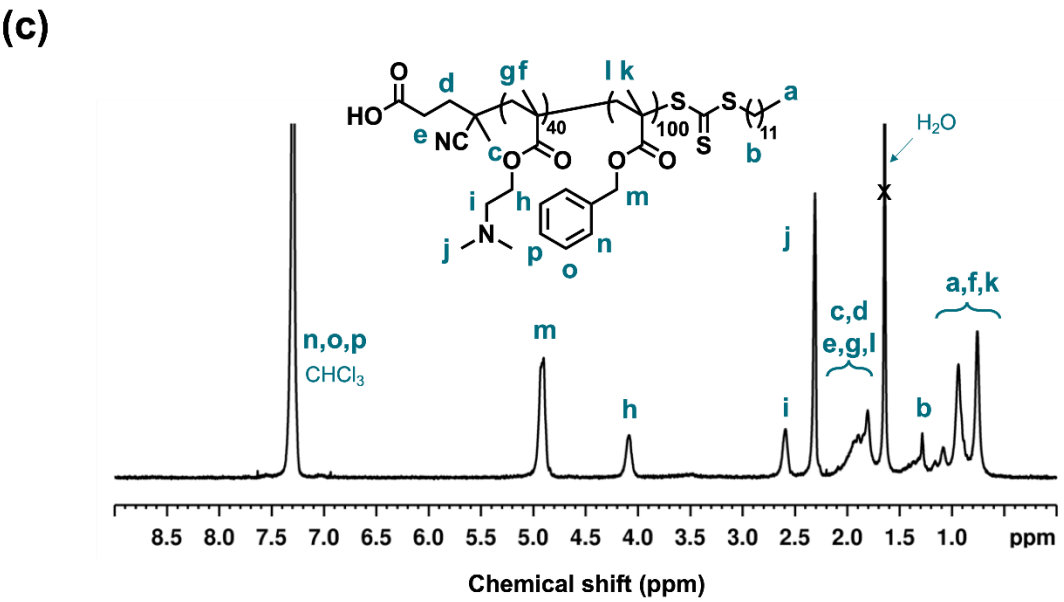

Figure 2. (a) RAFT polymerization of $PDMAEMA_{40}$ in isopropanol at 70 ºC, followed by RAFT dispersion polymerization of BzMA in anhydrous ethanol at 70 ºC with 20 wt% solid content to produce PDMAEMA-*b*-PBzMA diblock copolymers. (b) Size exclusion chromatograms of $PDMAEMA_{40}$ (PD, black), $PDMAEMA_{40}$-*b*-$PBzMA_{100}$ (PDB_1, blue) and $PDMAEMA_{40}$-*b*-$PBzMA_{200}$ (PDB_1, red), measured using dimethylacetamide (DMAc) as the eluent. (c) Representative ^1H NMR spectral assignment of PDMAEMA-*b*-PBzMA diblock copolymer using PDB_1, measured in $CDCl_3$.

PISA by RAFT dispersion polymerization was used to prepare worm-like and vesicular polymer nanostructures from PDMAEMA-*b*-PBzMA diblock copolymers in a one-pot system (Figure 2a). The diblock copolymer synthesis firstly involved the polymerization of linear PDMAEMA with low dispersity ($Đ$) of 1.17 (Table 1). ^1H NMR confirmed the formation of PDMAEMA (Figure S1). PDMAEMA with a degree of polymerization (DP) of 40 was specifically targeted as it is sufficiently long to maintain colloidal stability without impeding the fusion of nanoparticles. This is essential to avoid the formation of kinetically trapped spheres.[49] Subsequently, the solvophilic PDMAEMA was chain-extended with BzMA *via* RAFT dispersion polymerization at 70 ºC in anhydrous ethanol with 20 wt% solid content to prepare two well-defined diblock copolymers: $PDMAEMA_{40}$-*b*-$PBzMA_{100}$ (PDB_1) and $PDMAEMA_{40}$-*b*-$PBzMA_{200}$ (PDB_2). While styrene has been well-explored in many PISA systems, solvophobic PBzMA was selected as the core-forming polymer due to its relatively faster polymerization kinetics in which quantitative conversion can be achieved within 24 h. Under well-controlled polymerization conditions, diblock copolymers with low dispersity (Figure 2b) and quantitative conversions were yielded (Table 1). The representative ^1H NMR spectrum of a PDB diblock copolymer is shown in Figure 2c. PISA

nanostructures in worm-like and vesicular morphologies were produced with PDB_1 and PDB_2, respectively (Figures 3a and 3c, Figure S2). The as-prepared PDB_1 and PDB_2 templates are composed of a PDMAEMA shell and a PBzMA core, as shown in the transmission electron microscopy (TEM) images in Figures 3c and 3d. The worm-like PDB_1 have an average diameter of 24 nm while the vesicular PDB_2 are polydisperse in diameter, ranging from 100–200 nm. By manipulating the length of the PBzMA block, diverse morphologies were achieved ranging from spheres, worms to vesicles, underlining the versatility of PISA in producing nanostructures with various morphologies (Table S1, Figure S2, Figure S3). A change in reaction mixture opacity across these PISA dispersion polymerizations was observed after the polymerization (Figure S4). Particularly, free-standing gels were obtained for samples containing only worm-like nanostructures. This can be explained in terms of percolation theory that attributed this gelation behaviour to the multiple inter-worm contacts, as postulated by Lovett *et al.*[50] However, some studies attributed this to the physical entanglement of the anisotropic worms.[51,52]

Table 1. Characterization of polymers and PISA templates

Samples	Polymer composition	Conversion [a] (%)	M_n [b] (g×mol^{-1})	M_n [c] (g×mol^{-1})	Dispersity [d] ($Đ$)	Morphology [e]
PD	$PDMAEMA_{40}$	79	6700	5700	1.17	-
PDB_1	$PDMAEMA_{40}$-*b*-$PBzMA_{100}$	> 98	24300	24200	1.20	Worms
PDB_2	$PDMAEMA_{40}$-*b*-$PBzMA_{200}$	> 98	41900	38400	1.25	Vesicles

[a] Monomer conversion determined from changes in characteristic ^{1}H NMR integrals. [b] Theoretical molecular weight of the polymers determined from monomer conversion and initial feed ratio. [c,d] Number-average molecular weight and dispersity ($Đ = M_w/M_n$) determined from size exclusion chromatography (SEC) in DMAc calibrated using PMMA standards. [e] Morphologies observed using TEM and SEM at 0.2 wt% concentration.

Fabrication and characterization of TiO_2 nanostructures

We demonstrated the use of PDB_1 and PDB_2 as nanoreactors to structure TiO_2 into hybrids while maintaining the worm-like and vesicular template morphology. TALH was selected as the TiO_2 precursor as it is more stable in aqueous solution at room temperature than other commonly used titania precursors, such as titanium(IV) butoxide which is easily hydrolyzed when exposed to moisture in air. In addition, TALH has been shown to preferentially form anatase TiO_2 in earlier studies.[7–9,53,54] In battery research, anatase TiO_2 is specifically targeted due to its faster ion insertion kinetics and higher storage capacity compared to other TiO_2 polymorphs such as rutile and brookite.[55,56] More importantly, the negative charge on TALH allows selective coordination to the templates through its electrostatic interaction with the partially protonated PDMAEMA shell (pKa ~7.4) while the PBzMA core remains unloaded.

Worm-like PISA nanostructures are typically vulnerable to the presence of water due to same charge repulsion.[49] Many groups have studied the stabilization of worm-like nanostructures by either core or shell-crosslinking to allow further processing without disrupting the morphology.[57–60] However, our worm-like morphology was easily preserved by tuning the composition (ethanol/water solution) of the infiltration solution without needing any postpolymerization crosslinking. The TALH infiltration process of PDB_1 was carried out in an 80% v/v ethanol/water solution to ensure both the solubility of TALH and the integrity of worm-like nanostructure. A 50% v/v ethanol/water solution was initially used but we observed the formation of irregular morphologies that resulted from the morphological transition in the presence of high-water content (Figure S5). A 50% v/v ethanol/water solution was sufficient for infiltrating PBD_2 with TALH since vesicular PISA nanostructures were more resilient in an aqueous environment. The SEM images of the PDB hybrids, worm-like PDB_1/TALH and vesicular PDB_2/TALH are presented in

Figure S6, evidencing that TALH was only complexed to the PDMAEMA shells in both samples and that the infiltration process did not disrupt the delicate worm structure.

Previous studies employing TALH as a TiO_2 precursor have used the thermal hydrolysis process under reflux conditions to form anatase before performing further heat treatments, such as calcination.[7–9,53,54] We avoided the additional reflux step to prevent the in-solution phase transition of the polymer template and produced PDB_1-TiO_2/C and PDB_2-TiO_2/C directly through pyrolysis. During pyrolysis, the sp^2-hybridized polymeric template is carbonized to a thin carbon framework atop the TiO_2 nanocrystallites. The formation of such carbon framework has been proven to provide additional stability to well-defined nanostructures and improve the conductivity of anatase.[22,23,61–64] This leads to an enhancement of their electrochemical activity and stability when incorporated into LIBs as an anode. The calcination procedure can also be conducted in air to burn off the polymeric template, yielding pure (*sans* carbon) TiO_2 nanostructures, namely PDB_1-TiO_2 and PDB_2-TiO_2.

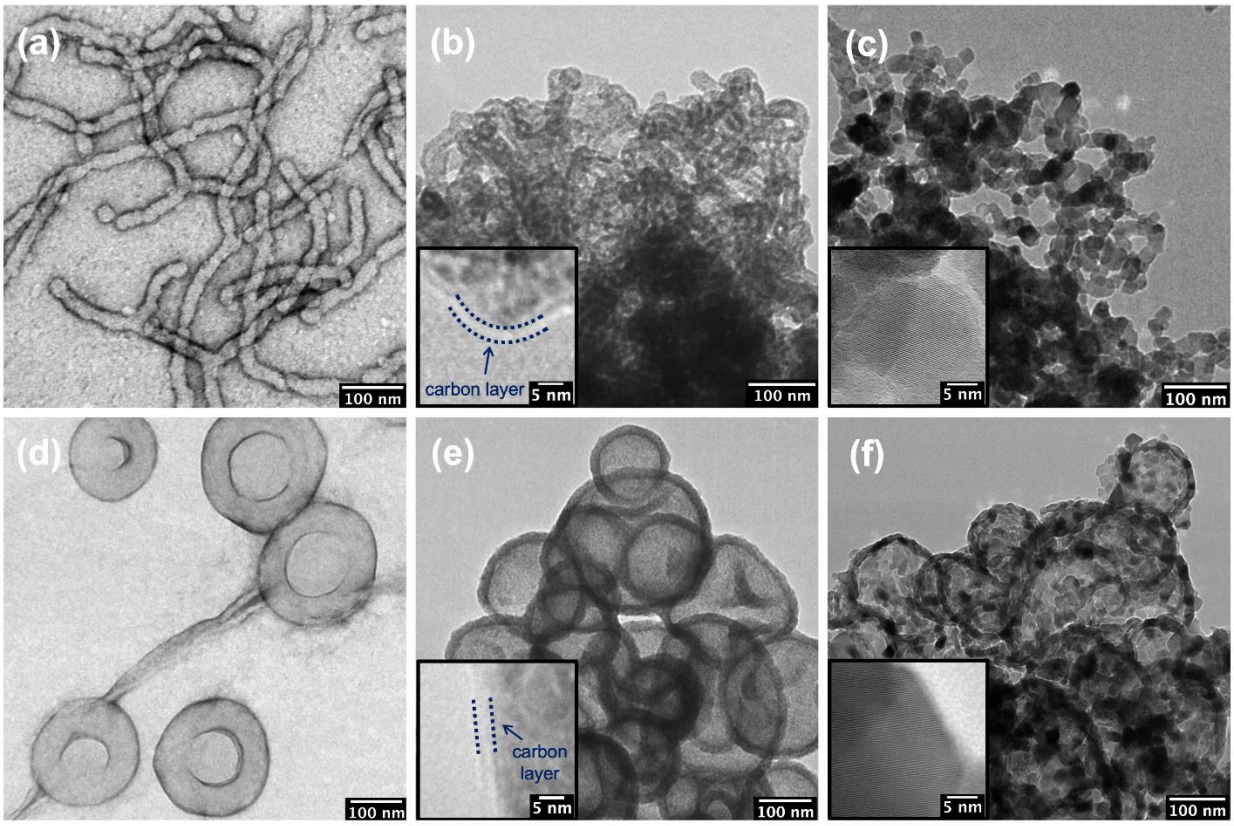

Figure 3. TEM images of as-prepared (a) PDB_1 and (d) PDB_2 polymers (0.2 wt%) negatively stained with 2% uranyl acetate solution. TEM images of the carbonized analogues; (b) PDB_1-TiO_2/C and (e) PDB_2-TiO_2/C, insets are the corresponding HRTEM images showing the carbon layer. TEM images of the calcined analogues; (c) PDB_1-TiO_2 and (f) PDB_2-TiO_2, insets show the corresponding HRTEM images. See Figures S7 and S8, for the full HRTEM micrographs of the insets in (b,e) and (c,f), respectively.

To characterize the as-synthesized PDB_1-TiO_2/C, PDB_2-TiO_2/C, PDB_1-TiO_2 and PDB_2-TiO_2, transmission electron microscopy (TEM), scanning electron microscopy (SEM), thermogravimetry analysis (TGA), powder X-ray diffraction (PXRD) as well as N_2 physisorption measurements, were performed. The characterization results are summarized in Table 2. Figures 3b and 3e show the TEM images of PDB_1-TiO_2/C and PDB_2-TiO_2/C, respectively, in which a

hollow core structure was observed within a TiO_2/C shell. An amorphous carbon layer as shown in the insets of Figures 3b and 3f, with a thickness of approximately 3 nm, was discernibly present surrounding the worm-like and vesicular TiO_2 (Figure S7). The SEM image in Figure 4a revealed that the normally fragile worm-like morphology of PDB_1 was successfully preserved in PDB_1/C after the heat treatment. In contrast, a bowl-shaped morphology was observed in PDB_2/C, creating a TiO_2 nanostructure with a wrinkled surface (Figure 4c). This is likely ascribed to the thin TiO_2 layer that resulted from the relatively short PDMAEMA stabilizing block shrinking during the loss of polymeric core in the carbonization process. Addition of more TALH or the use of a longer PDMAEMA stabilizing block may circumvent such shrinkage by thickening the shell layer.

The essence of our templating method also lies in the *in situ* generation of a carbon framework that provided a spatial confinement around the TiO_2, which suppressed the crystallite growth.[65] This was evidenced by the TEM images of the carbonized PDB_1-TiO_2/C (Figure 3b) and calcined PDB_1-TiO_2 (Figure 3c), revealing the loss of hollow core-shell structure after calcination in air as a result of TiO_2 crystallite overgrowth that eventually obstructed the hollow tube. While the hollow core of PDB_2-TiO_2 still remained, crystallite growth was similarly observed in the TEM image (Figure 3f). Nevertheless, the worm-like and vesicular morphologies of PDB_1-TiO_2 and PDB_2-TiO_2 were still preserved, as shown in the SEM images in Figures 4b and 4d. The corresponding PXRD patterns confirmed that crystalline anatase TiO_2 was produced in all TiO_2/C and TiO_2 analogues, with space group *I*4/*amd* and lattice parameters a = 0.3785 nm and c = 0.9515 nm (Figures 5a and 5b). The peak-broadening in the XRD patterns of the TiO_2/C analogues is ascribed to the small size of crystallites within the amorphous carbon matrix (5.1 nm for PDB_1-TiO_2/C, and 5.4 nm for PDB_2-TiO_2/C). Relatively sharp peaks were observed in the XRD patterns of bare (calcined) TiO_2 analogues due to the presence of larger-sized crystallites (30.9 nm and 35.9 nm,

respectively), as verified with their high-resolution TEM (HRTEM) images clearly showing crystal lattices (Figures 3d and 3f insets, Figure S8). By applying the Debye-Scherrer equation,[66] their average crystallite sizes were estimated and summarized in Table 2.

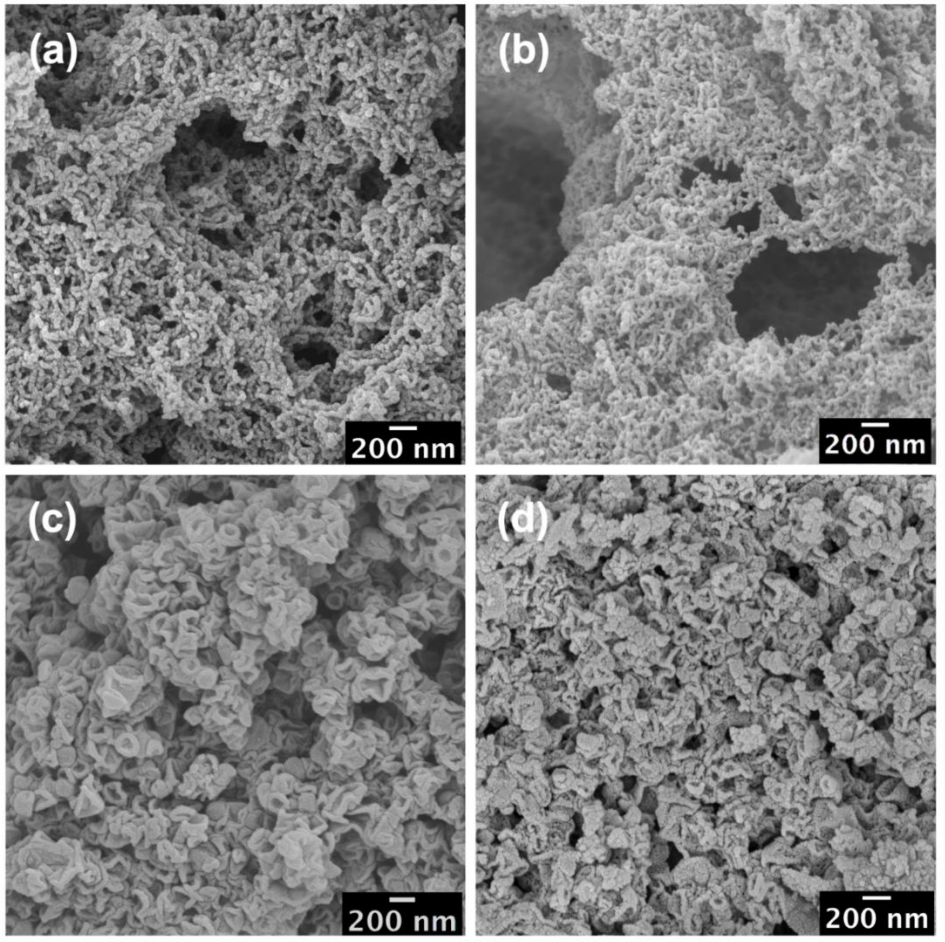

Figure 4. SEM images of (a) PDB_1-TiO_2/C, (b) PDB_1-TiO_2, (c) PDB_2-TiO_2/C and (d) PDB_2-TiO_2, sputtered with gold (15 nm).

TGA measurements were used to obtain the thermal decomposition profiles of the pristine PDB templates and the hybrid analogues (Figure 5c). Both worm-like and vesicular templates began their decomposition at approximately 180 ºC and finished slightly above 550 ºC. Hence, calcination temperature of the hybrid analogues at 650 ºC was selected to ensure complete removal

of the organic matter simultaneously with the crystallization of anatase. The TiO_2 weight contents in both PDB_1 and PDB_2 templates were determined to be 24%. The carbon contents in PDB_1-TiO_2/C and PDB_2-TiO_2/C were 23 wt% and 30 wt%, respectively (Figures S9a and S9b). The carbon content was expected to be larger for PDB_2 as it contains a much longer PBzMA block. Raman spectroscopy was performed to further study the structure of the carbon component of PDB-TiO_2/C samples (Figure S9c). In the spectra of both PDB-TiO_2/C samples, two peaks were observed at around 1360 cm^{-1} (D-band, disordered amorphous carbon) and 1580 cm^{-1} (G-band, ordered graphitic carbon). The peak intensity ratios of D-band and G-band (I_D/I_G) of PDB_1-TiO_2/C and PDB_2-TiO_2/C were calculated to be 1.25 and 1.19, respectively. These results indicate that the carbon species in the samples are in the form of a combined disordered amorphous and ordered graphical structure but dominated by the amorphous.

The porosities of the as-prepared TiO_2 nanostructures were analyzed using N_2 physisorption measurements at 77 K to evaluate their Brunauer-Emmett-Teller (BET)[67] surface areas (Figures 5d and 5e) and pore size distributions (Figure S10).[68] As-synthesized PDB_1/TALH and PDB_2/TALH showed low specific surface areas (15 $m^2\ g^{-1}$ and 7 $m^2\ g^{-1}$, respectively) and small pore volumes (0.029 $cm^3\ g^{-1}$ and 0.005 $cm^3\ g^{-1}$, respectively); consistent for organic/inorganic hybrid materials with remaining polymer occupying pores. After heat treatment to remove the templating agent, more accessible surfaces can be created. Despite having an increase in the pore volumes of PDB_1-TiO_2 (0.055 $cm^3\ g^{-1}$) and PDB_2-TiO_2 (0.030 $cm^3\ g^{-1}$), both materials recorded similarly low BET surface areas of 12 $m^2\ g^{-1}$ and 14 $m^2\ g^{-1}$, respectively. All four materials exhibited Type II isotherm behaviour with an H3 hysteresis loop, which are characteristic of nonporous or macroporous materials. We ascribed this to the formation of larger crystallites, which

is especially apparent for PDB_1-TiO_2, in which the loss of tube-like cavity in the worm-like structure was clearly shown in the TEM image (Figure 3c).

Carbonizing the templates has resulted in a significant increase in both the BET surface areas and the pore volumes of PDB_1-TiO_2/C (89 m^2 g^{-1}; 0.061 cm^3 g^{-1}) and PDB_2-TiO_2/C (86 m^2 g^{-1}; 0.051 cm^3 g^{-1}). Despite exhibiting Type II isotherm behaviour, the observation of an H4 hysteresis loop indicates that mesoporous and macropores were formed during the carbonization process. The uptake of N_2 at lower relative pressures increased from 0.1 to 1.0 mmol g^{-1}, indicating higher porosity of the material, including micropores. The higher porosity was also accompanied by an increase in the pore-size distributions (Figure S10). After carbonization, the small uniform pore widths of 1.5 nm became less uniform and ranged from 2.5–35 nm.

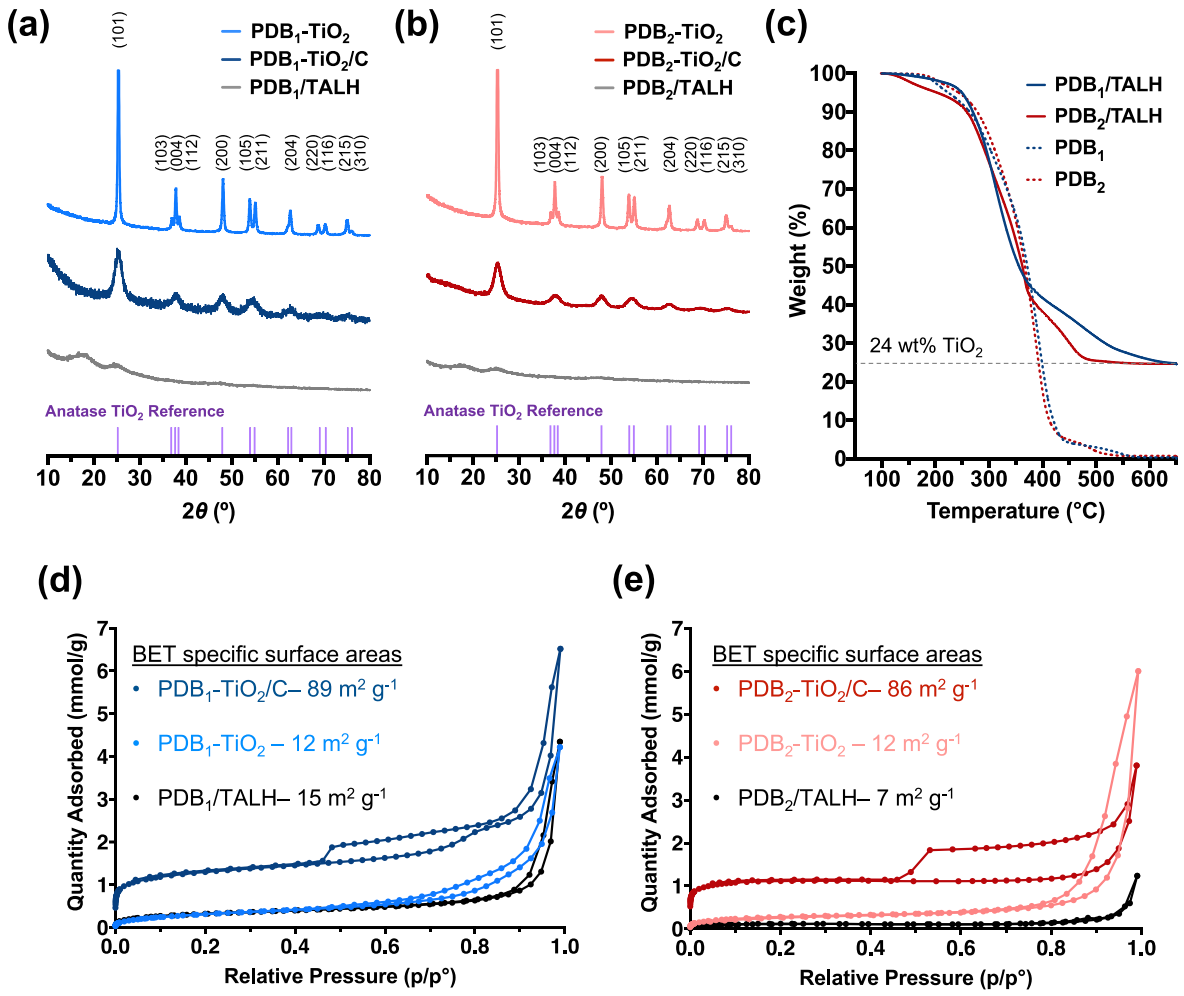

Figure 5. (a–b) Powder XRD patterns (Cu K_α, λ = 1.5406 Å) of the hybrid PDB/TALH, carbonized (PDB-TiO_2/C) and calcined (PDB-TiO_2) analogues templated using PDB_1 and PDB_2. The purple ticks mark the positions of the characteristic peaks of anatase TiO_2. (c) TGA of the pristine PDB_1 (blue, dashed line), PDB_2 (red, dashed line) and their hybrid analogues (red, blue, solid lines), respectively. (d–e) The N_2 physisorption isotherms, measured at 77 K, of the hybrid PDB/TALH, carbonized PDB-TiO_2/C and calcined PDB-TiO_2 analogues templated using PDB_1 and PDB_2.

Table 2. Summary of characterization data and electrochemical performance of the templated TiO_2 nanostructures

Samples	Specific surface area [a] ($m^2\ g^{-1}$)	Pore volume [b] ($cm^3\ g^{-1}$)	Crystallite size [c] (nm)	Stabilized Capacity [d] ($mAh\ g^{-1}$)	Capacity loss [e] (%)
PDB_1/TALH	15	0.029	n/a	n/a	n/a

PDB_1-TiO_2/C	89	0.061	5.4	370	9
PDB_1-TiO_2	12	0.055	35.9	215	26
PDB_2/TALH	7	0.005	n/a	n/a	n/a
PDB_2-TiO_2/C	86	0.051	5.1	285	1
PDB_2-TiO_2	15	0.030	30.9	224	37

[a] Specific surface area estimated from the BET theory. [b] Estimated total pore volume based on DFT. [c] Average crystallite size estimated from PXRD using the Debye-Scherrer equation. [d] The stabilized discharge capacity based on the cycle 5. [e] Capacity loss was determined by the discharge capacity loss at cycle 100 based on cycle 5. The cycling performance was recorded up to 100 cycles as the cycling stability was already established for the carbonized analogues.

Electrochemical performances as anode components

The mesoporous nanostructured carbon-coated anatase samples, namely, PDB_1-TiO_2/C and PDB_2-TiO_2/C, demonstrated an excellent electrochemical performance as anodes in LIBs. Detailed discussion on the discharge-charge voltage profiles can be found in Section S3 of the Supporting Information S3.

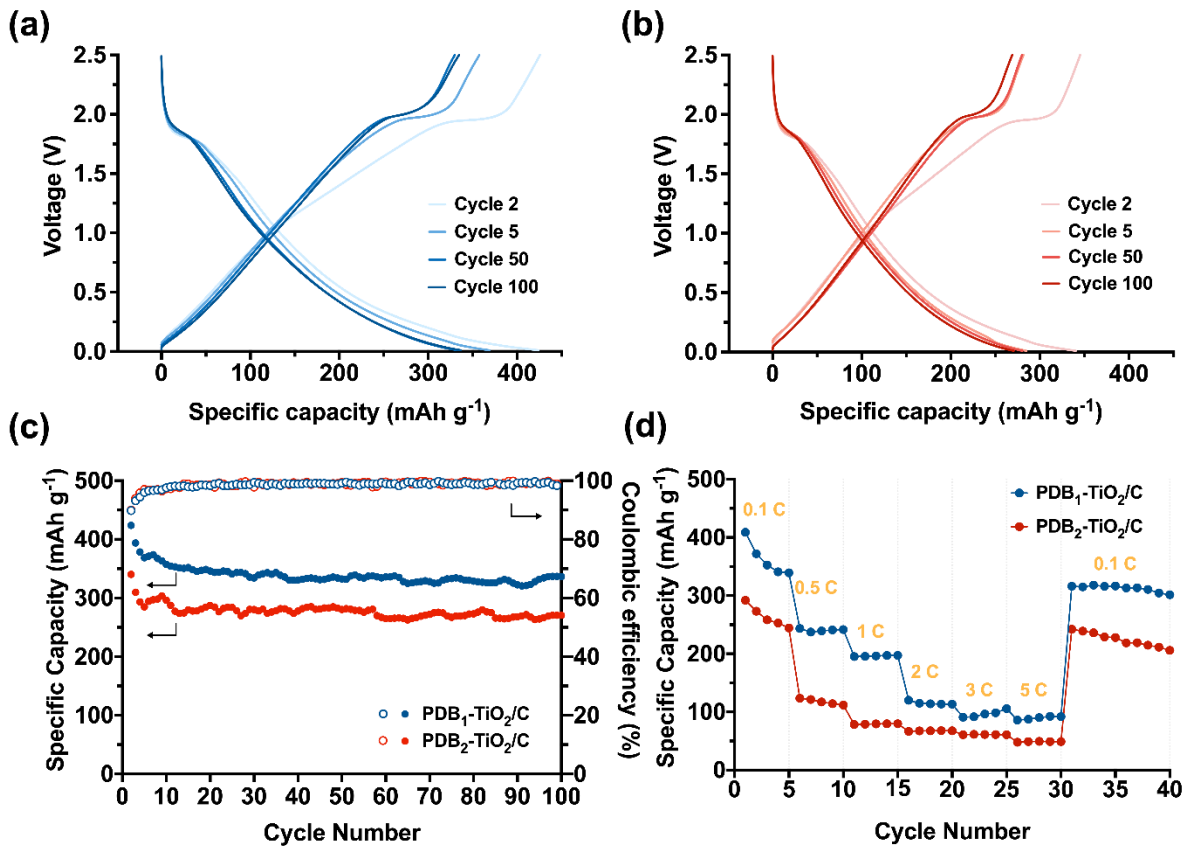

Figure 6. Charge/discharge voltage profiles of (a) PDB_1-TiO_2/C and (b) PDB_2-TiO_2/C in the cycles 2, 5, 50 and 100 at 0.1C. (c) The cycling performance of PDB_1-TiO_2/C (blue) and PDB_2-TiO_2/C (red) up to 100 cycles at 0.1 C (the plot fluctuation is caused by the room temperature change). (d) Rate performance at various C-rates.

PDB_1-TiO_2/C delivered a reversibly high discharge and charge capacities of 424 mAh g^{-1} and 426 mAh g^{-1}, respectively in the second cycle (Figure 6a), while those of PDB_2-TiO_2/C were 341 mAh g^{-1} and 342 mAh g^{-1} (Figure 6b). Higher capacities than the theoretical value of anatase (335 mAh g^{-1}) were achieved due to the carbon formed *in situ* during pyrolysis. This favourably contributed to Li^+ reactions as part of the absorption (on surfaces)/deposition (into nano-pores) mechanism (for amorphous carbon) and the intercalation mechanism (for graphitic carbon). Noticeable capacity losses for discharge/charge cycles were observed over five cycles for PDB_1-TiO_2/C (55

mAh g^{-1}/68 mAh g^{-1}) and for PDB_2-TiO_2/C (58 mAh g^{-1}/60 mAh g^{-1}). We ascribed these capacity losses to the electrolyte decomposition products blocking the micropores inside the amorphous carbon, leading to a progressive inability for Li-deposition over the short-term. This is evidenced by the higher capacity loss for discharge (Li^+-insertion) than for charge (Li^+-extraction) which indicates Li^+ ions get trapped in the cycled PDB_1-TiO_2/C and PDB_2-TiO_2/C electrodes. The electrolyte decomposition is a dominant side reaction in the initial discharge of an anode material, by which a protective passivation solid electrolyte interphase (SEI) film is formed on the surface of the anode.[69] Since both our carbon-coated anatase materials showed high specific surface areas (Table 2), the electrolyte decomposition in their batteries should be significant. As is expected, extremely high specific capacities of 842 mAh g^{-1} and 596 mAh $g^{-1}$for PDB_1-TiO_2/C and PDB_2-TiO_2/C, respectively, were observed in their initial discharge processes (Figure S12). The SEI film usually becomes stabilized chemically and morphologically in the first few cycles but may take more cycles for anodes with very large surface areas.[70] This SEI stabilization process is related to the above-mentioned ~~relatively major~~ capacity loss in the first five cycles, and to the minor loss in cycles 5 to 50, namely, ~38 mAh g^{-1} (9%) for PDB_1-TiO_2/C and ~5 mAh g^{-1} (1%) for PDB_2-TiO_2/C. The 50^{th} and 100^{th} cycles voltage profiles of PDB_1-TiO_2/C (Figure 6a) and PDB_2-TiO_2/C (Figure 6b) are fully overlapped, and as can be seen from the cycling performance results in Figure 6c, where almost no capacity fading was observed for both materials. PDB_1-TiO_2/C delivered a reversibly stable capacity of 331 mAh g^{-1} on average in cycles 50-100, and 271 mAh g^{-1} for PDB_2-TiO_2/C. Figure 6c shows that a high Coulombic Efficiency of nearly 100% was achieved by both materials from the fifth cycle onwards; demonstrating their lithiation-delithiation reactions were reversible in long-term cycling. In comparison to bare (*sans* carbon) PDB_1-TiO_2 and PDB_2-TiO_2

(Figure S11 c), and commercial nano-sized anatase (Figure S13), the cycling performances of our carbon-coated anatase nanomaterials were much superior.

Both PDB_1-TiO_2/C and PDB_2-TiO_2/C exhibited a good rate capability. As shown in Figure 6d, at large current densities of 0.5 C, 1 C, 2 C, 3 C and 5 C, PDB_1-TiO_2/C delivered high capacities of 363 mAh g^{-1}, 241 mAh g^{-1}, 196 mAh g^{-1}, 115 mAh g^{-1} and 97 mAh g^{-1}. PDB_2-TiO_2/C delivered respective capacities of 264 mAh g^{-1}, 118 mAh g^{-1}, 79 mAh g^{-1}, 67 mAh g^{-1} and 49 mAh g^{-1}. When the current density returned to 0.1 C, both materials completely recovered their higher capacities achieved at the low current density. Note that the capacity decline for both materials in the first five cycles at 0.1 C before the rate capability tests was caused by the SEI stabilization as discussed earlier. In contrast, PDB_1-TiO_2 and PDB_2-TiO_2 presented unsatisfying rate performances (see Figure S11d). The capacities of PDB_1-TiO_2 fell below 100 mAh g^{-1} at current densities larger than 1 C, while those of PDB_2-TiO_2 dropped to ~0 mAh g^{-1}. We attribute the superior attenuation on rate capability of the carbon-coated anatase materials to their finer TiO_2 crystallite size (see Table 2) and porous carbon framework, which better facilitate faster kinetics with Li^+ at high current densities.

The excellent electrochemical performances of our mesoporous carbon-coated anatase, *i.e.*, reversibly high capacities of 331 and 271 mAh g^{-1}, and superior cycling stability and rate capability, stem from the material morphologies accessible through the PISA templates. Firstly, the homogeneous distribution of anatase TiO_2 precursor in the polymer nanoreactors guaranteed the retention of nanostructure and morphology in the hybrid nanomaterial. Secondly, on pyrolysis, the self-inhibited growth of primary anatase particle by the *in situ* formed pyrolytic carbon framework led to an electrochemically favoured fine crystallite size of ~5 nm, and the formation of mesoporous nanomaterials with large surface area. The small crystallite size ensured a short Li^+

and electron diffusion pathway across the anatase bulk, while the large surface area provided a sufficient contact/reaction interface between the electrode and the electrolyte for Li^+ diffusion. Overall, these properties facilitated faster Li^+ kinetics within the mesoporous carbon-coated anatase nanomaterials. Lastly, the well-built mesoporous nanostructure can absorb the crystallographic stress generated by the volume change of the anatase unit cell during the Li^+-insertion and -extraction processes, maintaining the integrity of the TiO_2/C hybrids. The accumulated stress-induced electrode particle breakdown during cycling (*e.g.*, cracking) can be problematic, as new surfaces are continually generated which cause the electrolyte to decompose. PDB_1-TiO_2/C showed a higher capacity and better rate performance than PDB_2-TiO_2/C, despite their comparative anatase crystallite sizes of ~ 5 nm and specific surface areas of ~90 $m^2\ g^{-1}$. We ascribe this result to the higher carbon content of PDB_2-TiO_2/C (30 wt%) *vs.* PDB_1-TiO_2/C (23 wt%) and smaller pore volume (0.051 *vs.* 0.061 $cm^3\ g^{-1}$), which both cause less amounts of Li^+ ions to be stored in the amorphous carbon of PDB_2-TiO_2/C. The former factor decreases the Li-storability of the graphitic carbon due to slower diffusion kinetics of Li^+ in thicker carbon film, and the later reduces the Li-deposition capacity in carbon nanopores. The lower Li^+ diffusion kinetics of PDB_2-TiO_2/C can be clearly seen from its rate performance in Figure 6d. Differences in diffusion may further be attributed to morphological differences of the TiO_2/C anode components. A difference in charge-discharge capacity suggests that available net surface area has not been the sole influencer of lithium diffusion. Worm-like PDB_1-TiO_2/C exhibited an average pore width < 3 nm (Figure S10c), however also contained larger pore widths between 7-15 nm. These larger pore widths may be more suitable for the diffusion of Li^+ ions, which can readily permeate through the material. Worm-like PDB_1-TiO_2/C also showed greater accessible pore volume up to 0.12 $cm^3 g^{-1}$. By extension, the vesicular PDB_2TiO_2/C had its average pore width

reduced to < 2 nm, with only a small distribution of pores above 10 nm (Figure S10d). The pore volumes ranged from 0.025 to 0.09 cm^3g^{-1}, which were also smaller than those of the worm-like PDB_1TiO_2/C.

Conclusions

We successfully demonstrated PISA as a versatile method to synthesise mesoporous carbon-coated anatase with worm-like and vesicular morphologies using PDMAEMA-*b*-PBzMA diblock copolymer templates. The fabrication of carbon-coated anatase was achieved by leveraging the electrostatic interaction between TALH and the PDMAEMA shell in ethanolic aqueous solution, without the further need of chemical stabilization, such as crosslinking. The PISA nanoreactors in this work served both as guiding templates, but also as *in situ* carbon sources during pyrolysis to minimise nanocrystal sizes and further coat them with a carbon framework of tuneable morphology. When incorporated as anode materials into LIBs, the synergistic effects of the carbon framework around the mesoporous and nanocrystalline nanostructures resulted in the increased cycling stability and rate performance, especially compared to purely inorganic nanomaterials derived by calcination or from commercially sourced titania nanocrystals. We anticipate that the soft-templating method developed in this work can be widely applied in the synthesis of other carbon-coated metal oxides for a wide range of applications, not limited to battery research.

ASSOCIATED CONTENT

The Supporting Information is available free of charge on the ACS Publications website. Supporting Information includes materials, methods, and supplementary results, including polymer and hybrid characterization, electron microscopy and electrochemical performance studies.

AUTHOR INFORMATION

Corresponding Author

*Markus Müllner, E-Mail: markus.muellner@sydney.edu.au

Author Contributions

M. M. conceived the idea and supervised the research with C. D. L. Y. T. C and M. M. planned the experiments with the assistance of L. D. B. Y. T. C. developed the experimental setup with the assistance of L. D. B. Y. T. C. performed all the experiments and analyzed the data. Q. X. and Y. T. C. performed the electrochemical experiments and analyzed the data. H. L. contributed to the collection of TEM images. Y. T. C. and M. S. performed the N_2 physisorption measurements and analyzed the data. E. R. L. B. synthesized the CDTPA chain-transfer agent. All the authors discussed the results. Y. T. C., Q. X. and M. M. co-wrote the manuscript with inputs from all the authors. The authors declare no conflict of interest.

Funding Sources

M.M. and C. D. L. acknowledge the Australian Research Council for their Future Fellowship (FT200100185, M.M.) and Discovery Projects (DP200100959, C. D. L; DP220100452, M.M.).

ACKNOWLEDGMENTS

This research was facilitated by access to Sydney Analytical, a core research facility at the University of Sydney. The authors acknowledge the technical and scientific assistance of Sydney Microscopy & Microanalysis, The University of Sydney node of Microscopy Australia. We acknowledge Prof. Deanna D'Alessandro for use of the 3-Flex Gas Adsorption Analyzer and Dr.

Michelle Wood for performing the Raman measurements. Y.T.C. is a grateful recipient of a University of Sydney International Scholarship (USydIS). Q.X. thanks the Australian Institute of Nuclear Science and Engineering for the Early Career Researcher (ECR) Grant and the Sydney Nano Institute for the ECR Support Fund. This work was also supported in part by a CSIRO CERC Postdoctoral Fellowship (L. D. B.).

REFERENCES

(1) Wu, H. B.; Chen, J. S.; Hng, H. H.; Lou, W. X. Nanostructured Metal Oxide-Based Materials as Advanced Anodes for Lithium-Ion Batteries. *Nanoscale* **2012**, *4* (8), 2526. https://doi.org/10.1039/c2nr11966h.

(2) Kment, S.; Riboni, F.; Pausova, S.; Wang, L.; Wang, L.; Han, H.; Hubicka, Z.; Krysa, J.; Schmuki, P.; Zboril, R. Photoanodes Based on TiO2 and α-Fe2O3 for Solar Water Splitting - Superior Role of 1D Nanoarchitectures and of Combined Heterostructures. *Chem. Soc. Rev.* **2017**, *46* (12), 3716–3769. https://doi.org/10.1039/c6cs00015k.

(3) Bhati, V. S.; Kumar, M.; Banerjee, R. Gas Sensing Performance of 2D Nanomaterials/Metal Oxide Nanocomposites: A Review. *J. Mater. Chem. C* **2021**, *9* (28), 8776–8808. https://doi.org/10.1039/D1TC01857D.

(4) Lai, Y.; Lin, L.; Pan, F.; Huang, J.; Song, R.; Huang, Y.; Lin, C.; Fuchs, H.; Chi, L. Bioinspired Patterning with Extreme Wettability Contrast on TiO $_2$ Nanotube Array Surface: A Versatile Platform for Biomedical Applications. *Small* **2013**, *9* (17), 2945–2953. https://doi.org/10.1002/smll.201300187.

(5) Weeks, J. A.; Sun, H. H.; Srinivasan, H. S.; Burrow, J. N.; Guerrera, J. V.; Meyerson, M. L.; Dolocan, A.; Heller, A.; Mullins, C. B. Facile Synthesis of a Tin Oxide-Carbon Composite Lithium-Ion Battery Anode with High Capacity Retention. *ACS Appl. Energy Mater.* **2019**, *2* (10), 7244–7255. https://doi.org/10.1021/acsaem.9b01205.

(6) Yuan, T.; Soule, L.; Zhao, B.; Zou, J.; Yang, J.; Liu, M.; Zheng, S. Recent Advances in Titanium Niobium Oxide Anodes for High-Power Lithium-Ion Batteries. *Energy and Fuels* **2020**, *34* (11), 13321–13334. https://doi.org/10.1021/acs.energyfuels.0c02732.

(7) Müllner, M.; Lunkenbein, T.; Schieder, M.; Gröschel, A. H.; Miyajima, N.; Förtsch, M.; Breu, J.; Caruso, F.; Müller, A. H. E. Template-Directed Mild Synthesis of Anatase Hybrid Nanotubes within Cylindrical Core–Shell–Corona Polymer Brushes. *Macromolecules* **2012**, *45* (17), 6981–6988. https://doi.org/10.1021/ma301232m.

(8) Schöttle, M.; Xia, Q.; Cheng, Y. T.; Shepherd, N. D.; Ling, C. D.; Müllner, M. Integrated Polyphenol-Based Hydrogel Templating Method for Functional and Structured Oxidic Nanomaterials. *Chem. Mater.* **2020**, *32* (11), 4716–4723. https://doi.org/10.1021/acs.chemmater.0c01306.

(9) McRae, O. F.; Xia, Q.; Tjaberings, S.; Gröschel, A. H.; Ling, C. D.; Müllner, M. Block Copolymer-directed Synthesis of Porous Anatase for Lithium-ion Battery Electrodes. *J. Polym. Sci. Part A Polym. Chem.* **2019**, *57* (18), 1890–1896. https://doi.org/10.1002/pola.29312.

(10) Cho, J. S.; Hong, Y. J.; Kang, Y. C. Design and Synthesis of Bubble-Nanorod-Structured

Fe2O3-Carbon Nanofibers as Advanced Anode Material for Li-Ion Batteries. *ACS Nano* **2015**, *9* (4), 4026–4035. https://doi.org/10.1021/acsnano.5b00088.

(11) Wei, H.; Rodriguez, E. F.; Hollenkamp, A. F.; Bhatt, A. I.; Chen, D.; Caruso, R. A. High Reversible Pseudocapacity in Mesoporous Yolk–Shell Anatase TiO2/TiO2(B) Microspheres Used as Anodes for Li-Ion Batteries. *Adv. Funct. Mater.* **2017**, *27* (46), 1–9. https://doi.org/10.1002/adfm.201703270.

(12) Poolakkandy, R. R.; Menamparambath, M. M. Soft-Template-Assisted Synthesis: A Promising Approach for the Fabrication of Transition Metal Oxides. *Nanoscale Adv.* **2020**, *2* (11), 5015–5045. https://doi.org/10.1039/D0NA00599A.

(13) Huang, L.; Kruk, M. Versatile Surfactant/Swelling-Agent Template for Synthesis of Large-Pore Ordered Mesoporous Silicas and Related Hollow Nanoparticles. *Chem. Mater.* **2015**, *27* (3), 679–689. https://doi.org/10.1021/cm5028749.

(14) Li, C.; Li, Q.; Kaneti, Y. V.; Hou, D.; Yamauchi, Y.; Mai, Y. Self-Assembly of Block Copolymers towards Mesoporous Materials for Energy Storage and Conversion Systems. *Chem. Soc. Rev.* **2020**, *49* (14), 4681–4736. https://doi.org/10.1039/D0CS00021C.

(15) Wei, W.; Samad, L.; Choi, J. W.; Joo, Y.; Way, A.; Arnold, M. S.; Jin, S.; Gopalan, P. Synthesis of Molybdenum Disulfide Nanowire Arrays Using a Block Copolymer Template. *Chem. Mater.* **2016**, *28* (11), 4017–4023. https://doi.org/10.1021/acs.chemmater.6b01453.

(16) Long, Y.-Z.; Li, M.-M.; Gu, C.; Wan, M.; Duvail, J.-L.; Liu, Z.; Fan, Z. Recent Advances in Synthesis, Physical Properties and Applications of Conducting Polymer Nanotubes and Nanofibers. *Prog. Polym. Sci.* **2011**, *36* (10), 1415–1442. https://doi.org/10.1016/j.progpolymsci.2011.04.001.

(17) Kim, M. P.; Ku, K. H.; Kim, H. J.; Jang, S. G.; Yi, G.-R.; Kim, B. J. Surface Intaglio Nanostructures on Microspheres of Gold-Cored Block Copolymer Spheres. *Chem. Mater.* **2013**, *25* (21), 4416–4422. https://doi.org/10.1021/cm402868q.

(18) Connal, L. A.; Lynd, N. A.; Robb, M. J.; See, K. A.; Jang, S. G.; Spruell, J. M.; Hawker, C. J. Mesostructured Block Copolymer Nanoparticles: Versatile Templates for Hybrid Inorganic/Organic Nanostructures. *Chem. Mater.* **2012**, *24* (21), 4036–4042. https://doi.org/10.1021/cm3011524.

(19) Fischer, M. G.; Hua, X.; Wilts, B. D.; Gunkel, I.; Bennett, T. M.; Steiner, U. Mesoporous Titania Microspheres with Highly Tunable Pores as an Anode Material for Lithium Ion Batteries. *ACS Appl. Mater. Interfaces* **2017**, *9* (27), 22388–22397. https://doi.org/10.1021/acsami.7b03155.

(20) Li, J.; Ho, Y.; Ahmed, M. M. M.; Liang, H.; Kuo, S. Mesoporous Carbons Templated by PEO-PCL Block Copolymers as Electrode Materials for Supercapacitors. *Chem. – A Eur. J.* **2019**, *25* (44), 10456–10463. https://doi.org/10.1002/chem.201901724.

(21) Zhu, Y.; Zhao, Y.; Ma, J.; Cheng, X.; Xie, J.; Xu, P.; Liu, H.; Liu, H.; Zhang, H.; Wu, M.; Elzatahry, A. A.; Alghamdi, A.; Deng, Y.; Zhao, D. Mesoporous Tungsten Oxides with Crystalline Framework for Highly Sensitive and Selective Detection of Foodborne Pathogens. *J. Am. Chem. Soc.* **2017**, *139* (30), 10365–10373. https://doi.org/10.1021/jacs.7b04221.

(22) Jo, C.; Kim, Y.; Hwang, J.; Shim, J.; Chun, J.; Lee, J. Block Copolymer Directed Ordered Mesostructured TiNb2O 7 Multimetallic Oxide Constructed of Nanocrystals as High Power Li-Ion Battery Anodes. *Chem. Mater.* **2014**, *26* (11), 3508–3514. https://doi.org/10.1021/cm501011d.

(23) Wu, R.; Shen, S.; Xia, G.; Zhu, F.; Lastoskie, C.; Zhang, J. Soft-Templated Self-Assembly

of Mesoporous Anatase TiO2/Carbon Composite Nanospheres for High-Performance Lithium Ion Batteries. *ACS Appl. Mater. Interfaces* **2016**, *8* (31), 19968–19978. https://doi.org/10.1021/acsami.6b03733.

(24) Wong, C. K.; Qiang, X.; Müller, A. H. E.; Gröschel, A. H. Self-Assembly of Block Copolymers into Internally Ordered Microparticles. *Prog. Polym. Sci.* **2020**, *102*, 101211. https://doi.org/10.1016/j.progpolymsci.2020.101211.

(25) D'Agosto, F.; Rieger, J.; Lansalot, M. RAFT-Mediated Polymerization-Induced Self-Assembly. *Angew. Chemie Int. Ed.* **2020**, *59* (22), 8368–8392. https://doi.org/10.1002/anie.201911758.

(26) Rieger, J. Guidelines for the Synthesis of Block Copolymer Particles of Various Morphologies by RAFT Dispersion Polymerization. *Macromol. Rapid Commun.* **2015**, *36* (16), 1458–1471. https://doi.org/10.1002/marc.201500028.

(27) Penfold, N. J. W.; Yeow, J.; Boyer, C.; Armes, S. P. Emerging Trends in Polymerization-Induced Self-Assembly. *ACS Macro Lett.* **2019**, *8* (8), 1029–1054. https://doi.org/10.1021/acsmacrolett.9b00464.

(28) Zhang, W.-J.; Hong, C.-Y.; Pan, C.-Y. Polymerization-Induced Self-Assembly of Functionalized Block Copolymer Nanoparticles and Their Application in Drug Delivery. *Macromol. Rapid Commun.* **2019**, *40* (2), 1800279. https://doi.org/10.1002/marc.201800279.

(29) Lv, F.; An, Z.; Wu, P. Scalable Preparation of Alternating Block Copolymer Particles with Inverse Bicontinuous Mesophases. *Nat. Commun.* **2019**, *10* (1). https://doi.org/10.1038/s41467-019-09324-5.

(30) Blanazs, A.; Madsen, J.; Battaglia, G.; Ryan, A. J.; Armes, S. P. Mechanistic Insights for Block Copolymer Morphologies: How Do Worms Form Vesicles? *J. Am. Chem. Soc.* **2011**, *133* (41), 16581–16587. https://doi.org/10.1021/ja206301a.

(31) Zhang, W. J.; Hong, C. Y.; Pan, C. Y. Formation of Hexagonally Packed Hollow Hoops and Morphology Transition in RAFT Ethanol Dispersion Polymerization. *Macromol. Rapid Commun.* **2015**, *36* (15), 1428–1436. https://doi.org/10.1002/marc.201500122.

(32) Gao, P.; Cao, H.; Ding, Y.; Cai, M.; Cui, Z.; Lu, X.; Cai, Y. Synthesis of Hydrogen-Bonded Pore-Switchable Cylindrical Vesicles via Visible-Light-Mediated RAFT Room-Temperature Aqueous Dispersion Polymerization. *ACS Macro Lett.* **2016**, *5* (12), 1327–1331. https://doi.org/10.1021/acsmacrolett.6b00796.

(33) Pontes da Costa, A.; Nunes, D. R.; Tharaud, M.; Oble, J.; Poli, G.; Rieger, J. Palladium(0) Nanoparticles Embedded in Core-Shell Nanogels as Recoverable Catalysts for the Mizoroki-Heck Reaction. *ChemCatChem* **2017**, *9* (12), 2167–2175. https://doi.org/10.1002/cctc.201601645.

(34) Cardozo, A. F.; Julcour, C.; Barthe, L.; Blanco, J. F.; Chen, S.; Gayet, F.; Manoury, E.; Zhang, X.; Lansalot, M.; Charleux, B.; D'Agosto, F.; Poli, R.; Delmas, H. Aqueous Phase Homogeneous Catalysis Using Core-Shell Nanoreactors: Application to Rhodium-Catalyzed Hydroformylation of 1-Octene. *J. Catal.* **2015**, *324*, 1–8. https://doi.org/10.1016/j.jcat.2015.01.009.

(35) Mable, C. J.; Gibson, R. R.; Prevost, S.; McKenzie, B. E.; Mykhaylyk, O. O.; Armes, S. P. Loading of Silica Nanoparticles in Block Copolymer Vesicles during Polymerization-Induced Self-Assembly: Encapsulation Efficiency and Thermally Triggered Release. *J. Am. Chem. Soc.* **2015**, *137* (51), 16098–16108. https://doi.org/10.1021/jacs.5b10415.

(36) Blackman, L. D.; Oo, Z. Y.; Qu, Y.; Gunatillake, P. A.; Cass, P.; Locock, K. E. S.

Antimicrobial Honey-Inspired Glucose-Responsive Nanoreactors by Polymerization-Induced Self-Assembly. *ACS Appl. Mater. Interfaces* **2020**, *12* (10), 11353–11362. https://doi.org/10.1021/acsami.9b22386.

(37) Derry, M. J.; Mykhaylyk, O. O.; Armes, S. P. A Vesicle-to-Worm Transition Provides a New High-Temperature Oil Thickening Mechanism. *Angew. Chemie* **2017**, *129* (7), 1772–1776. https://doi.org/10.1002/ange.201609365.

(38) Chang, J.; Zhang, W.; Hong, C. Template-Directed Fabrication of Anatase TiO2 Hollow Nanoparticles and Their Application in Photocatalytic Degradation of Methyl Orange. *Chinese J. Chem.* **2017**, *35* (6), 1016–1022. https://doi.org/10.1002/cjoc.201600890.

(39) Bennett, T. M.; He, G.; Larder, R. R.; Fischer, M. G.; Rance, G. A.; Fay, M. W.; Pearce, A. K.; Parmenter, C. D. J.; Steiner, U.; Howdle, S. M. Clean Block Copolymer Microparticles from Supercritical CO 2 : Universal Templates for the Facile and Scalable Fabrication of Hierarchical Mesostructured Metal Oxides. *Nano Lett.* **2018**, *18* (12), 7560–7569. https://doi.org/10.1021/acs.nanolett.8b03044.

(40) Teo, G. H.; Kuchel, R. P.; Zetterlund, P. B.; Thickett, S. C. Polymer-Inorganic Hybrid Nanoparticles of Various Morphologies: Via Polymerization-Induced Self Assembly and Sol-Gel Chemistry. *Polym. Chem.* **2016**, *7* (43), 6575–6585. https://doi.org/10.1039/c6py01447j.

(41) Zhang, Y.; Wang, Z.; Matyjaszewski, K.; Pietrasik, J. Versatile PISA Templates for Tailored Synthesis of Nanoparticles. *Eur. Polym. J.* **2019**, *110*, 49–55. https://doi.org/10.1016/j.eurpolymj.2018.11.014.

(42) Blanazs, A.; Ryan, A. J.; Armes, S. P. Predictive Phase Diagrams for RAFT Aqueous Dispersion Polymerization: Effect of Block Copolymer Composition, Molecular Weight, and Copolymer Concentration. *Macromolecules* **2012**, *45* (12), 5099–5107. https://doi.org/10.1021/ma301059r.

(43) Jones, E. R.; Semsarilar, M.; Wyman, P.; Boerakker, M.; Armes, S. P. Addition of Water to an Alcoholic RAFT PISA Formulation Leads to Faster Kinetics but Limits the Evolution of Copolymer Morphology. *Polym. Chem.* **2016**, *7* (4), 851–859. https://doi.org/10.1039/c5py01795e.

(44) Zhang, W.-J.; Hong, C.-Y.; Pan, C.-Y. Fabrication and Characterization of Silica Nanotubes with Controlled Dimensions. *J. Mater. Chem. A* **2014**, *2* (21), 7819. https://doi.org/10.1039/c4ta00465e.

(45) Wei, T.-T.; Wang, F.-F.; Li, X.-Z.; Zhang, J.-H.; Zhu, Y.-R.; Yi, T.-F. Towards High-Performance Battery Systems by Regulating Morphology of TiO2 Materials. *Sustain. Mater. Technol.* **2021**, *30*, e00355. https://doi.org/10.1016/j.susmat.2021.e00355.

(46) Song, T.; Paik, U. TiO 2 as an Active or Supplemental Material for Lithium Batteries. *J. Mater. Chem. A* **2016**, *4* (1), 14–31. https://doi.org/10.1039/C5TA06888F.

(47) Liang, S.; Wang, X.; Cheng, Y. J.; Xia, Y.; Müller-Buschbaum, P. Anatase Titanium Dioxide as Rechargeable Ion Battery Electrode - A Chronological Review. *Energy Storage Mater.* **2022**, *45* (August 2021), 201–264. https://doi.org/10.1016/j.ensm.2021.11.023.

(48) Zhu, K.; Feng, W.; Xue, Z.; Sun, M.; Wu, S.; Jing, Z.; Yu, Y. In Situ Conformal Carbon Coating for Constructing Hierarchical Mesoporous Titania/Carbon Spheres as High-Rate Lithium-Ion Battery Anodes. *ACS Sustain. Chem. Eng.* **2022**, *10* (33), 10955–10965. https://doi.org/10.1021/acssuschemeng.2c03017.

(49) Jones, E. R.; Semsarilar, M.; Wyman, P.; Boerakker, M.; Armes, S. P. Addition of Water to an Alcoholic RAFT PISA Formulation Leads to Faster Kinetics but Limits the Evolution of

Copolymer Morphology. *Polym. Chem.* **2016**, *7* (4), 851–859. https://doi.org/10.1039/C5PY01795E.
(50) Lovett, J. R.; Derry, M. J.; Yang, P.; Hatton, F. L.; Warren, N. J.; Fowler, P. W.; Armes, S. P. Can Percolation Theory Explain the Gelation Behavior of Diblock Copolymer Worms? *Chem. Sci.* **2018**, *9* (35), 7138–7144. https://doi.org/10.1039/C8SC02406E.
(51) Dreiss, C. A. Wormlike Micelles: Where Do We Stand? Recent Developments, Linear Rheology and Scattering Techniques. *Soft Matter* **2007**, *3* (8), 956. https://doi.org/10.1039/b705775j.
(52) Cates, M. E. Reptation of Living Polymers: Dynamics of Entangled Polymers in the Presence of Reversible Chain-Scission Reactions. *Macromolecules* **1987**, *20* (9), 2289–2296. https://doi.org/10.1021/ma00175a038.
(53) Müllner, M.; Lunkenbein, T.; Miyajima, N.; Breu, J.; Müller, A. H. E. A Facile Polymer Templating Route toward High-Aspect-Ratio Crystalline Titania Nanostructures. *Small* **2012**, *8* (17), 2636–2640. https://doi.org/10.1002/smll.201200738.
(54) Li, H.; Mao, X.; Wang, H.; Geng, Z.; Xiong, B.; Zhang, L.; Liu, S.; Xu, J.; Zhu, J. Kinetically Dependent Self-Assembly of Chiral Block Copolymers under 3D Confinement. *Macromolecules* **2020**, *53* (11), 4214–4223. https://doi.org/10.1021/acs.macromol.0c00406.
(55) Fröschl, T.; Hörmann, U.; Kubiak, P.; Kucerová, G.; Pfanzelt, M.; Weiss, C. K.; Behm, R. J.; Hüsing, N.; Kaiser, U.; Landfester, K.; Wohlfahrt-Mehrens, M. High Surface Area Crystalline Titanium Dioxide: Potential and Limits in Electrochemical Energy Storage and Catalysis. *Chem. Soc. Rev.* **2012**, *41* (15), 5313–5360. https://doi.org/10.1039/c2cs35013k.
(56) Su, D.; Dou, S.; Wang, G. Anatase TiO 2 : Better Anode Material Than Amorphous and Rutile Phases of TiO 2 for Na-Ion Batteries. *Chem. Mater.* **2015**, *27* (17), 6022–6029. https://doi.org/10.1021/acs.chemmater.5b02348.
(57) He, J.; Xu, Q.; Tan, J.; Zhang, L. Ketone-Functionalized Polymer Nano-Objects Prepared via Photoinitiated Polymerization-Induced Self-Assembly (Photo-PISA) Using a Poly(Diacetone Acrylamide)-Based Macro-RAFT Agent. *Macromol. Rapid Commun.* **2019**, *40* (2). https://doi.org/10.1002/marc.201800296.
(58) Zhang, L.; Lu, Q.; Lv, X.; Shen, L.; Zhang, B.; An, Z. In Situ Cross-Linking as a Platform for the Synthesis of Triblock Copolymer Vesicles with Diverse Surface Chemistry and Enhanced Stability via RAFT Dispersion Polymerization. *Macromolecules* **2017**, *50* (5), 2165–2174. https://doi.org/10.1021/acs.macromol.6b02651.
(59) Zhang, B.; Lv, X.; Zhu, A.; Zheng, J.; Yang, Y.; An, Z. Morphological Stabilization of Block Copolymer Worms Using Asymmetric Cross-Linkers during Polymerization-Induced Self-Assembly. *Macromolecules* **2018**, *51* (8), 2776–2784. https://doi.org/10.1021/acs.macromol.8b00246.
(60) Byard, S. J.; Williams, M.; McKenzie, B. E.; Blanazs, A.; Armes, S. P. Preparation and Cross-Linking of All-Acrylamide Diblock Copolymer Nano-Objects via Polymerization-Induced Self-Assembly in Aqueous Solution. *Macromolecules* **2017**, *50* (4), 1482–1493. https://doi.org/10.1021/acs.macromol.6b02643.
(61) Lee, J.; Jung, Y. S.; Warren, S. C.; Kamperman, M.; Oh, S. M.; Disalvo, F. J.; Wiesner, U. Direct Access to Mesoporous Crystalline TiO2/Carbon Composites with Large and Uniform Pores for Use as Anode Materials in Lithium Ion Batteries. *Macromol. Chem. Phys.* **2011**, *212* (4), 383–390. https://doi.org/10.1002/macp.201000687.
(62) Yang, Z.; Du, G.; Guo, Z.; Yu, X.; Chen, Z.; Guo, T.; Liu, H. TiO2(B)@carbon Composite

Nanowires as Anode for Lithium Ion Batteries with Enhanced Reversible Capacity and Cyclic Performance. *J. Mater. Chem.* **2011**, *21* (24), 8591. https://doi.org/10.1039/c0jm03873c.

(63) Ha, J. U.; Lee, J.; Abbas, M. A.; Lee, M. D.; Lee, J.; Bang, J. H. Designing Hierarchical Assembly of Carbon-Coated TiO 2 Nanocrystals and Unraveling the Role of TiO 2 /Carbon Interface in Lithium-Ion Storage in TiO 2. *ACS Appl. Mater. Interfaces* **2019**, *11* (12), 11391–11402. https://doi.org/10.1021/acsami.8b21705.

(64) Qian, R.; Lu, H.; Yao, T.; Xiao, F.; Shi, J.-W.; Cheng, Y.; Wang, H. Hollow TiNb 2 O 7 Nanospheres with a Carbon Coating as High-Efficiency Anode Materials for Lithium-Ion Batteries. *ACS Sustain. Chem. Eng.* **2022**, *10* (1), 61–70. https://doi.org/10.1021/acssuschemeng.1c04712.

(65) Lee, J.; Christopher Orilall, M.; Warren, S. C.; Kamperman, M.; DiSalvo, F. J.; Wiesner, U. Direct Access to Thermally Stable and Highly Crystalline Mesoporous Transition-Metal Oxides with Uniform Pores. *Nat. Mater.* **2008**, *7* (3), 222–228. https://doi.org/10.1038/nmat2111.

(66) Holzwarth, U.; Gibson, N. The Scherrer Equation versus the "Debye-Scherrer Equation." *Nat. Nanotechnol.* **2011**, *6* (9), 534–534. https://doi.org/10.1038/nnano.2011.145.

(67) Brunauer, S.; Emmett, P. H.; Teller, E. Adsorption of Gases in Multimolecular Layers. *J. Am. Chem. Soc.* **1938**, *60* (2), 309–319. https://doi.org/10.1021/ja01269a023.

(68) Landers, J.; Gor, G. Y.; Neimark, A. V. Density Functional Theory Methods for Characterization of Porous Materials. *Colloids Surfaces A Physicochem. Eng. Asp.* **2013**, *437*, 3–32. https://doi.org/10.1016/j.colsurfa.2013.01.007.

(69) Wang, A.; Kadam, S.; Li, H.; Shi, S.; Qi, Y. Review on Modeling of the Anode Solid Electrolyte Interphase (SEI) for Lithium-Ion Batteries. *npj Computational Materials*. Nature Publishing Group December 2018. https://doi.org/10.1038/s41524-018-0064-0.

(70) Heiskanen, S. K.; Kim, J.; Lucht, B. L. Generation and Evolution of the Solid Electrolyte Interphase of Lithium-Ion Batteries. *Joule* **2019**, *3* (10), 2322–2333. https://doi.org/10.1016/j.joule.2019.08.018.

Table of Content Graph